Imaging complex model catalysts in action: From surface science towards industrial practice using high-pressure scanning tunneling microscopy

Mom, R.V.

Chapter 4

The growth and stability of Au surface oxides on WO3/Au(111) and ReO3/Au(111) inverse model catalysts

Oxide-supported gold catalysts enable oxidation reactions at mild temperatures, providing a unique set of pathways for green chemistry. To investigate whether Au surface oxides may play a role in the catalysis, we studied their autocatalytic formation and stability on WO_3/Au(111) and ReO_3/Au(111) inverse model catalysts. We find that Au surface oxides are thermodynamically stable over a wide range of catalytically relevant conditions. The formation of the surface oxides requires initial seeds of AuO_x on our model catalysts, but proceeds autocatalically from there on, with an O_2 dissociation barrier that is mainly entropic.

4.1 Introduction

Despite its reputation as an inert metal, oxide-supported gold has the unparalleled ability to catalyze oxidation reactions at room temperature[1]. This gives Au-based catalysts great potential for applications in a.o. automotive catalysis[1], the pharmaceutical industry[2], and biorefineries[3]. Nonetheless, commercialization of Au catalysts has proven difficult due to their high cost and poor stability[4]. It is vital therefore to capture the essence of the current-day Au catalysts as a design parameter in future development.

The search for the essential features that give oxide-supported Au its tremendous activity has shown that many factors can play a role, depending on the type of catalyst and the employed conditions. Examples include the Au particle size[5–9], the presence of cationic Au[10–15], the particle-support interaction[9,10,16], and the water concentration in the feed[9,17,18].

To unravel the underlying principles that determine the importance of these factors, a vast number of mechanistic studies has emerged, predominantly focused on the oxidation of CO. It is generally agreed that CO adsorbs on the Au particles[5,12,13,19,20]. Oxygen activation is often modeled as adsorption at the gold-support perimeter in the form of molecular[21–24] or support lattice oxygen[25,26], which subsequently reacts with CO. Such models are supported by the observation that the CO oxidation activity scales linearly with the number of perimeter sites[17,26].

However, there is increasing evidence suggesting that gold can play a more extensive role in storing and dissociating oxygen. Fujitani *et al.*[17] showed that the linear scaling with perimeter sites breaks down at slightly elevated temperatures for Au/TiO_2 catalysts. Instead, the observed reactivity scaled with the total number of Au surface sites, suggesting that oxygen is distributed over the entire surface of the Au particles. Indeed, density functional theory (DFT) calculations indicate that the formation of Au surface oxides on both the Au-gas[27–30] and Au-support interface[12,13,31] are thermodynamically favorable in an oxygen atmosphere. Furthermore, it was shown that Au surface oxides catalyze oxygen dissociation[32]. Spectroscopic studies confirm the existence of oxidized Au species in supported Au catalysts[10,11,14,33,34], yet leave their nature and catalytic role unclear. Specifically, it is unclear whether Au oxides are formed at the gas-Au interface or only at the Au-support interface, where they may reside as mere spectator species.

Here, we investigate the autocatalytic formation and thermodynamic stability of Au surface oxides at the gas-Au interface on WO_3/Au(111) and ReO_3/Au(111) inverse model catalysts. In contrast to practical catalysts, these inverted models have the oxides present in nanoparticle form and gold as the support. This allows us to specifically study surface oxides on the dominant surface orientation of Au

nanoparticles, (111), and their interaction with oxide materials. Using scanning tunneling microscopy (STM) and X-ray photoelectron spectroscopy (XPS), we studied Au oxide formation in O_2 pressures of 10^{-5} mbar to 500 mbar at temperatures up to 423 K. We find that WO_3 and ReO_3 have a minor effect on the behavior of AuO_x. The stability and reaction kinetics of the surface oxides are analyzed in terms of simple thermodynamic considerations.

4.2 Methods

To study the WO_3/Au(111) and ReO_3/Au(111) catalysts both in ultrahigh vacuum (UHV) and at elevated pressures, we used the ReactorSTM[35] developed in our group. With its high-pressure flow cell inside a UHV system, it allows us to prepare and characterize model catalysts in vacuum and subsequently expose the surface to a controlled high-pressure environment without air exposure. When the reactor seal is removed, the STM can be operated in UHV for vacuum studies. The system is also equipped with a commercial photoelectron spectrometer (SPECS Phoibos) for XPS analysis.

4.2.1 Model catalyst preparation

Clean, atomically smooth Au(111) was prepared by cycles of 1 keV Ar^+ bombardment and annealing at 900 K. The cleanliness of the surface was confirmed by STM and XPS. The WO_3 and ReO_3 were deposited on the support by reactive evaporation using an e-beam evaporator (Oxford Applied Research). To accomplish this, a rod of the respective metal was held at approximately 1100 K during exposure to $1x10^{-5}$ mbar O_2, creating volatile oxides (see Ref. [36] for more details on this method).

4.2.2 Generation of Au oxide precoverage

While O_2 dissociation faces large energy barriers on Au(111)[37], Au surface oxides readily form when strong oxidizing agents are used, such as electron stimulated NO_2[38] and ozone[39]. We chose to generate small amounts of atomic oxygen using a thoriated iridium filament in $1x10^{-5}$ mbar O_2. At its working temperature of approximately 1750 K, thoriated iridium provides a very low O_2 dissociation rate, thus allowing for a controlled experiment were the vast majority of the surface oxide is formed via O_2 dissociation on AuO_x seeds.

4.2.3 XPS analysis

XPS measurements were carried out in UHV with the X-ray incidence angle at 54° off normal and electron collection along the surface normal. After a Tougaard background subtraction, the Re 4f and O 1s spectra were fitted with the Gaussian/Lorentzian curves implemented in the CasaXPS[40] software package. A Shirley background subtraction was used for the Au 4f spectra. Re and O coverages, expressed in monolayers with the packing

density of Au(111), were calculated based on the Re 4f/Au 4f and O 1s/Au 4f intensity ratios using:

$$\theta_{Re} = \frac{I_{Re}}{I_{Au}} \cdot \frac{RSF_{Au-4f}}{RSF_{Re-4f}} \cdot \frac{1}{1 - e^{-d_{111}/\lambda}} \quad (4.1)$$

$$\theta_{O} = \frac{I_{O}}{I_{Au}} \cdot \frac{RSF_{Au-4f}}{RSF_{O-1s}} \cdot \frac{1}{1 - e^{-d_{111}/\lambda}} \quad (4.2)$$

In equations 4.1 and 4.2, I_x is the measured XPS intensity of the respective element, RSF_x the relative sensitivity factor of the probed transition[40], d_{111} the Au(111) layer spacing, and λ the attenuation length of Au 4f photoelectrons in Au[41]. To establish the equations, we have assumed that the Re and O atoms on the surface do not attenuate the Au 4f signal. The last term in equations 4.1 and 4.2 gives the effective number of Au monolayers that is probed in the Au 4f spectrum, thus compensating for the fact that XPS probes deeper than the first layer of the Au(111) surface.

4.3 Results and discussion

We first investigated the structure of WO_3 and ReO_3 on a clean Au(111) sample. After deposition at room temperature, WO_3 adopts an amorphous island structure (see Figure 4.1a). Depending on the state of the STM tip, the apparent height of the islands can be both positive and negative. ReO_3 adopts the same structure as WO_3 (not shown), which is not surprising in view of their chemical similarity. The persistence of the herringbone reconstruction of the Au(111) substrate[42] during WO_3 and ReO_3 deposition, which is performed in $1x10^{-5}$ mbar O_2, shows that neither of these oxides is able to catalyze the formation of Au oxides. As both WO_3 and ReO_3 are well-known oxidation catalysts, this is likely due to their inability to transfer oxygen atoms from the oxide to the Au surface rather than to ineffective O_2 dissociation.

When the WO_3/Au(111) sample is annealed at 527 K, the oxide islands crystallize (see Figure 4.1b). The structure consists of paired rows with a periodicity of 1.6 nm, indicating a large unit cell. This is likely the result of a lattice mismatch between the tungsten oxide and the Au(111) substrate. The amount of oxide on the surface was strongly reduced during the annealing. Meanwhile dark stains appeared in the Au terraces, indicating surface alloying (see Figure 4.1b and Figure 4.7 in the Supporting Information). This highlights the reducible nature of WO_3 when in contact with gold.

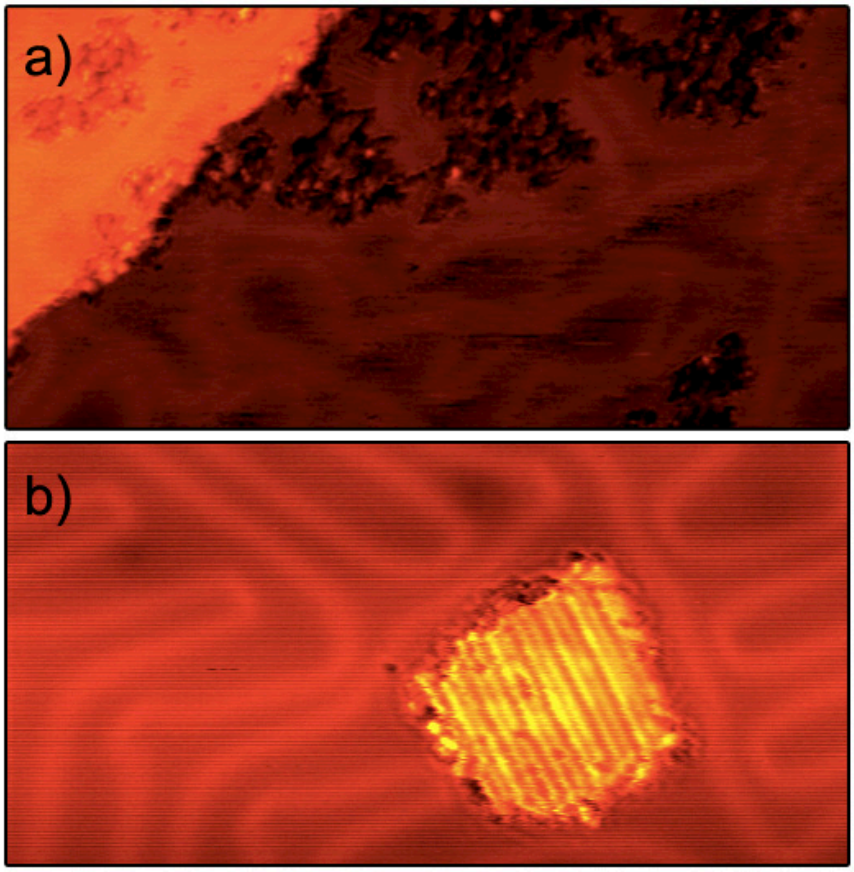

Figure 4.1: WO_3 deposited on Au(111). a) As deposited at room temperature. 70 nm x 35 nm, U_s = 1.5 V, I_t = -120 pA. b) After annealing at 567 K. Notice the vague dark stains in the herringbone reconstruction at the top of the image, which indicate surface alloying. 40 nm x 20 nm, U_s = 2 V, I_t = -95 pA.

4.3.1 Disordered surface oxide

At room temperature, exposing WO_3/Au(111) and ReO_3/Au(111) to a $1x10^{-5}$ mbar O_2/atomic O mixture generates disordered structures (see Figure 4.2). After 15 minutes of exposure, XPS indicates an oxygen coverage of 0.23 ML on a 0.012 ML ReO_3/Au(111) sample. This should be considered as a lower bound due to X-ray induced desorption (see Figure 4.8 in the Supporting Information). Similar to observations after NO_2 or O_3 dosing[38,39], the STM images in Figure 4.2 indicate a highly corroded Au surface, implying that Au adatoms were recruited from the terraces to be incorporated into a surface oxide. Both WO_3 and ReO_3 dissolve into the surface oxide, without clearly affecting its structure. This is corroborated by the position of the O 1s peak (529.7 eV), which is unchanged with respect to pure O/Au(111) prepared at room temperature[38].

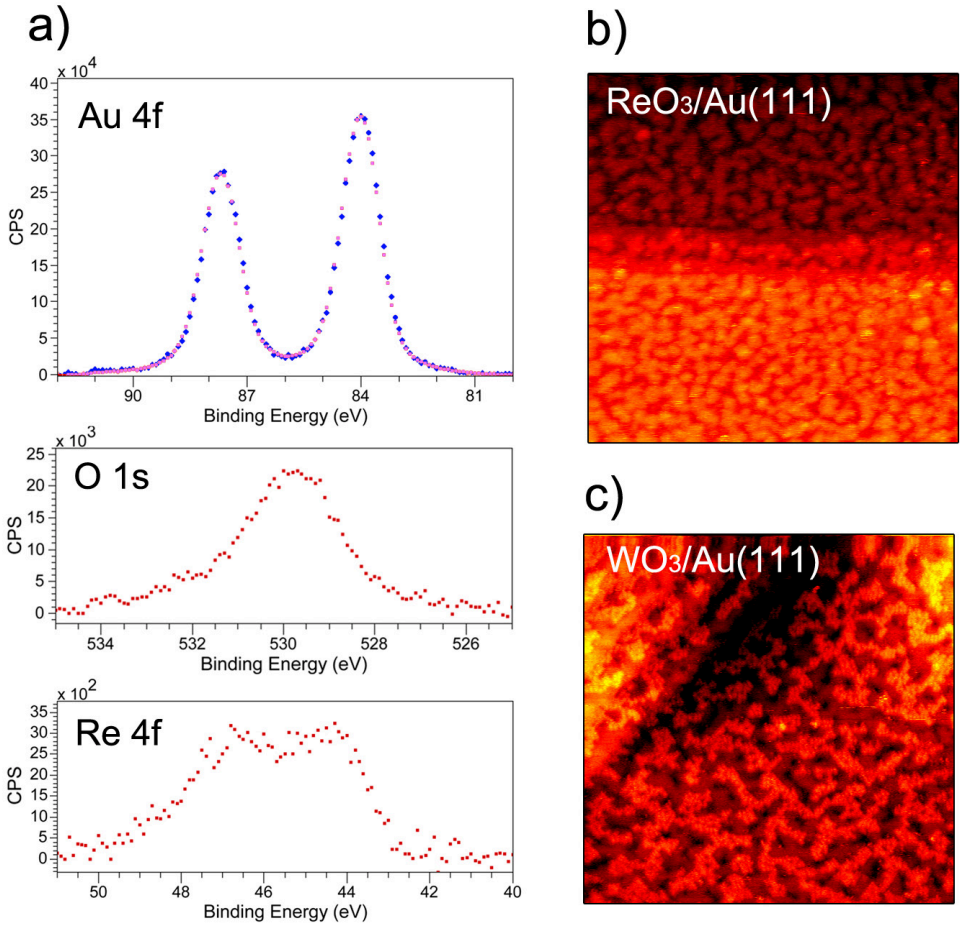

Figure 4.2: XPS and STM data of ReO_3/Au(111) and WO_3/Au(111) after exposure to 1x10^{-5} mbar O_2/O at room temperature. a) Background-subtracted XPS spectra of ReO_3/Au(111) (red) and clean Au(111) (blue). The intensities of the Au 4f spectra of clean Au(111) and ReO_3/Au(111) where set equal at the $4f_{7/2}$ peak. b) STM image of ReO_3/Au(111) 80 nm x 80 nm, U_s = -1V, I_t = 35 pA. c) STM image of WO_3/Au(111) 80 nm x 80 nm, U_s = -1V, I_t = 35 pA.

The Au 4f spectrum in 4.2 shows no sign of oxidized Au, which would appear as a small shoulder on the higher binding energy side of the metallic Au peak. This is similar to the case of sulfur adsorption on Au(111), where Au adatom incorporation also leaves the Au oxidation state unchanged[38,43]. Hence, whether one assigns the observed structure to a surface oxide or to an oxygen-induced reconstruction is a matter of definition. It should however be clear that the structure observed in Figure 4.2 is distinctly different from the weak chemisorption of oxygen on the perfect Au(111) surface[5,29].

The observation that surface oxides at the Au-gas interface need not contain detectably oxidized Au has important consequences for the interpretation of spectroscopic data of Au catalysts. XPS or X-ray absorption spectra on Au transitions alone may not tell the full story. Furthermore, the beam damage after exposure to weak lab source X-rays suggests that the surface oxides may decompose abruptly under synchrotron X-ray irradiation. For vibrational spectroscopy, it is also uncertain whether the Au surface oxide has a sufficiently distinct chemical nature with respect to bare Au to allow for resolved CO vibration peaks. These considerations highlight the importance of direct observations on well-defined CO oxidation catalysts that allow for unambiguous assignment of catalytic intermediates.

4.3.2 Surface oxide in 500 mbar O_2

To investigate the behavior of the gold surface oxides under catalytically relevant pressures, we exposed WO_3/Au(111) and ReO_3/Au(111) catalysts with a small initial Au oxide coverage to oxygen pressures up to 500 mbar. Figure 4.3a shows ReO_3/Au(111) during exposure to 500 mbar O_2. The streaky appearance of the surface indicates fast surface dynamics. This implies that there is no densely packed crystalline surface oxide phase on the Au terraces, but rather disordered Au oxide structures that can assemble and disassemble with high rates.

Over time, islands with rod shapes appear on the surface (see Figures 3 and S3 in the Supporting Information), showing that the high-pressure conditions facilitate the formation of a new phase with respect to the vacuum situation described in the previous section. The islands crystallize further when left in vacuum after the high-pressure exposure. Figures 3b and c show the resulting structure, which appears to be identical to the one observed on Au(111) after ozone treatment at 400K[39]. At room temperature, such an ozone treatment yields a disordered structure similar to Figures 2b and c. Hence, the main effect induced by high pressure is the increase in mobility of oxygen-containing species.

The preparation process of the initial AuO_x seeds prior to the high-pressure experiment created vacancy islands in the Au terraces. These vacancy islands remain when the surface is left in vacuum for 24 hours. However, during the high-pressure exposure the density of vacancy islands clearly decreases within 2 hours (see Figures 4.9 and 4.10 in the Supporting Information). Meanwhile, the total area of the vacancy islands appears to remain constant, although this was difficult to quantify due to the streaky character of the images (standard deviation: ±37%). We conclude that the high-pressure conditions induce accelerated ripening.

The observation of a constant total vacancy island area suggests that the dynamic species on the Au terraces do not contain Au adatoms. This is corroborated by the observation that no new vacancy islands are formed, which did occur at lower O_2 pressure at room temperature (see previous section). Since the rod shaped Au oxide islands can only communicate with the vacancy islands and step edges via the

dynamic species on the terraces, we conclude that the Au oxide islands also do not contain Au adatoms.

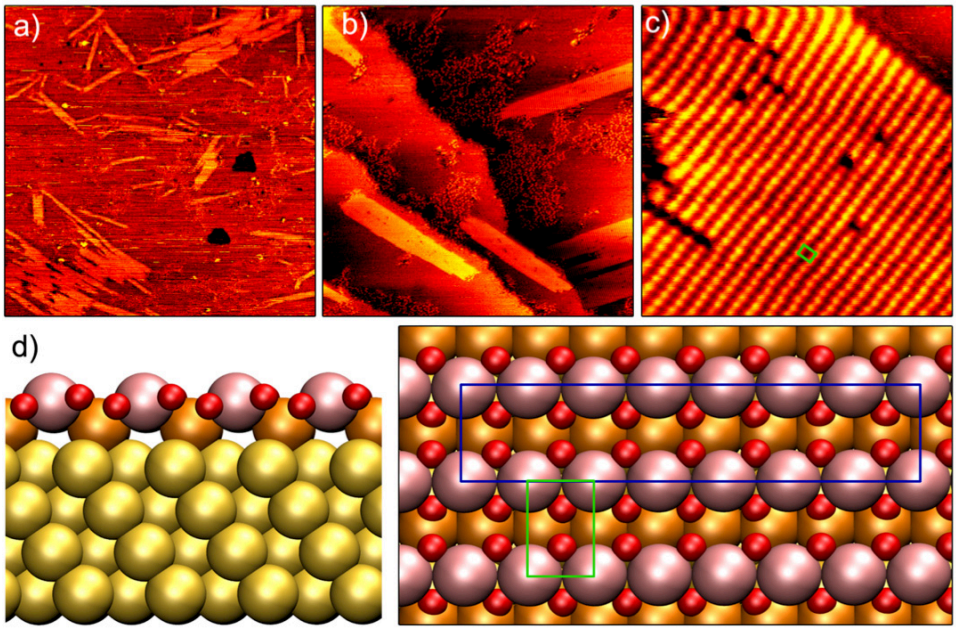

Figure 4.3: Au surface oxide formed on ReO_3/Au(111) in 500 mbar O_2 at room temperature. a) *In situ* image, 160 nm x 160 nm, U_s = 2 V, I_t = -120 pA. b) Image after crystallization in UHV for 17 hours, 80 nm x 80 nm, U_s = 1 V, I_t = -100 pA. c) High-resolution image of the structure in panel b, 10 nm x 10 nm, U_s = 0.42 V, I_t = -200 pA. The green rectangle indicates the observed unit cell d) Proposed structure of the Au surface oxide. Left: cross sectional view, parallel to the lifted Au rows. Right: top view, in which the lifted Au rows run from left to right. The unit cell is indicated in blue, while green indicates the local unit cell that is primarily observed in the experiment. Bulk Au, interface Au, oxidic Au, and O atoms are colored gold, orange, pink, and red, respectively.

The Au oxide islands shown in Figure 4.3 have a 0.49±0.02 nm x 0.33±0.007 nm rectangular unit cell with its short axis lying along the close-packed direction of the Au surface. While the long axis of the unit cell fits well with the Au lattice, the short axis is 14% larger than the Au nearest neighbor distance. Due to this mismatch with the Au(111) lattice, one may expect a buckling in the AuO_x islands. On the large-scale image in Figure 4.3b, no such buckling is observed. At the atomic scale in Figure 4.3c however, it is clear that small sideways deviations from the perfect regular lattice occur. The displacements do not appear to follow a completely regular pattern, which could indicate that defects and island edges impose long-range stress in the islands. The measured height of the islands was 0.14 nm, independent of the applied tip-sample bias. This is well below the Au(111) step height of 0.23 nm, which is consistent with the earlier indication that the surface oxide does not contain Au adatoms.

Based on the geometrical arguments above, the Au surface oxide structures proposed in the literature[27,30], and the similarity to the case of Pt(111)[44–47], we propose the structure depicted in Figure 4.3d for the Au oxide islands. In this structure Au atoms are lifted out of the terrace by 4 oxygen atoms, as was also observed in *ab initio* molecular dynamics simulations[27]. Thus, oxide rows are formed, similar to those predicted[44] and observed[46,47] on Pt(111). DFT calculations on a similar structure on Pt(110) showed that the dense packing of oxygen atoms in the oxide rows creates compressive stress, driving the rows to expand along the row direction[48]. This can explain the lattice mismatch of 14% along the row direction observed in our experiments.

The expansion of the Au oxide rows necessitates the expulsion of Au atoms. Based on the observed island coverage, this would amount to 0.5-1% of a monolayer, which is approximately half the vacancy island coverage. One may expect that part of the adatoms are used to fill the vacancy islands, while the rest attaches to step edges. We suggest that the decrease in vacancy island coverage lies within the 37% standard deviation of the measurement.

4.3.3 Low coverage needle oxide

To test the stability of the Au surface oxide, we performed experiments at various temperatures. At 423 K, a crystalline "needle"-shaped Au oxide with a modest coverage is formed during the $1x10^{-5}$ mbar O_2/O exposure (see Figure 4.4). This result was independent of the exposure time (see Section 4.8 in the Supporting Information), from which we conclude that the needle phase is an equilibrium structure. The WO_3 and ReO_3 islands in Figure 4.4 were deposited at 500 K, resulting in a partially crystalline island structure with a bright appearance.

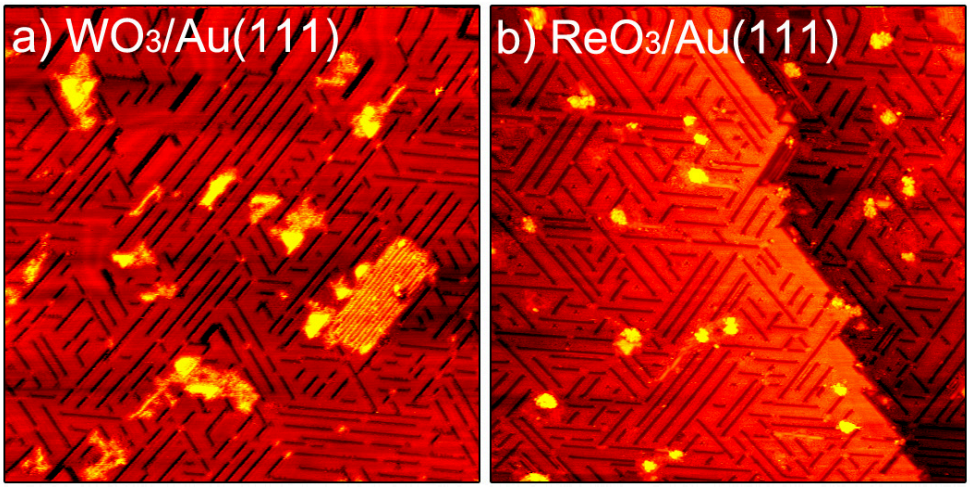

Figure 4.4: WO_3/Au(111) and ReO_3/Au(111) after exposure to $1x10^{-5}$ mbar O_2 mbar at 423 K. a) WO_3/Au(111) 80 nm x 80 nm, U_s = 1V, I_t = -125 pA. b) ReO_3/Au(111) 80 nm x 80 nm, U_s = 2V, I_t = -130 pA.

When left in vacuum at room temperature, the needle phase disappears within approximately 24 hours (see Figure 4.5). This disappearance is not observed for the disordered Au oxide, nor for the Au oxide islands. Hence, the barrier for desorption must be lower for the needle structure, indicating that it is either less stable, or more active in catalyzing O_2 adsorption/desorption.

The needles shown in Figure 4.4 follow the close-packed directions of the Au(111) lattice and occur as single or double oxide rows. Similarly, for Pt(111) it was shown that at intermediate coverage the oxide rows form a honeycomb network of single to triple rows[46]. Their proposed structure was almost identical to those in the Au oxide island structure. Therefore, it is tempting to interpret the needles as isolated or paired rows of the island oxide structure. In this case however, there must be a stabilizing force that prevents the oxide rows from assembling into islands. A possible candidate for this would be stress relaxation in the Au surface. Figures 4.4 and 4.5 show that the herringbone reconstruction is lifted in the close vicinity of the oxide needles, but remains elsewhere. Hence, it appears that the oxide needles can relief compressive stress in the Au surface, similar to the herringbone reconstruction[42]. As a result, there is a driving force for the needles to remain isolated up to the coverage where the herringbone reconstruction is fully lifted.

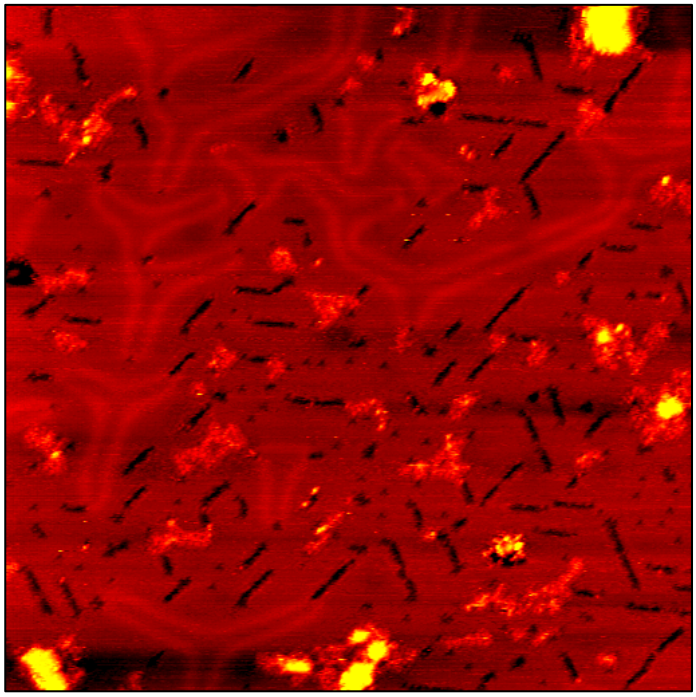

Figure 4.5: Low coverage AuO_x on WO_3/Au(111) after exposure to $1x10^{-5}$ mbar O_2 mbar at 423 K and 18.5 h in vacuum, 80 nm x 80 nm, U_s = 2 V, I_t = -95 pA

In Figure 4.4, it appears as if WO_3 and ReO_3 have little effect on the Au needle oxide other than disturbing its long-range order. At low AuO_x coverage however, it becomes clear that the Au surface oxide is stabilized in the vicinity of WO_3. Figure 4.5 shows that the locations of the two oxides correlate. The correlation is not perfect however, indicating that the stabilization is subtle. Nonetheless, this result suggests that Au oxides may form preferably on the Au-support perimeter in industrial Au catalysts, as was also found in a DFT study on Au nanoparticles on TiO_2[13].

4.3.4 Energetics of Au surface oxide

O_2/O exposure at temperatures higher than 423 K did not result in oxide growth. Under the assumption that the atomic oxygen did not significantly influence the equilibrium oxygen coverage, one can use this transition temperature between formation and absence of formation of the oxide to estimate the oxide formation enthalpy. At the transition temperature, the free energy of formation is zero. This means that the contributions of the enthalpy (ΔH_{ads}) and entropy ($T\Delta S_{ads}$) of formation cancel (see Figure 4.6a). Assuming that oxygen loses all entropy upon adsorption, $-\Delta S_{ads}$ equals the gas phase entropy of oxygen ($S_{O2(g)}$). With this assumption, $T\Delta S_{ads}$ = -1.6 eV per O_2 molecule under the applied conditions[49]. Hence, we find a formation enthalpy of the oxide of -1.6 eV per O_2 molecule. This value is corroborated by experiments from Deng *et al.*[32], who showed that oxygen can be adsorbed up to 0.4 ML on O-precovered Au(111) in $1x10^{-7}$ mbar O_2 at 400 K, which implies the same -1.6 eV formation enthalpy when analyzed using the above arguments. This validates our assumption that the atomic oxygen present in the gas phase during our experiment did not significantly affect the stability range of the Au surface oxide.

The formation enthalpy derived above can be used to determine the stability of surface oxides as a function of temperature and pressure. The Au oxide coverage (θ) can be obtained as a function of temperature (T) and pressure (P) through a Langmuir model[50]:

$$\frac{\theta}{\theta_{max}} = \frac{\sqrt{KP}}{\sqrt{KP}+1} \tag{4.3}$$

$$K = e^{-(\Delta H_{ads} + TS^0_{O_2(g)})/k_B T} \tag{4.4}$$

$S^0_{O2(g)}$ designates the standard entropy of gaseous O_2, given at standard pressure (P^0, 1 bar). Note that we have included the temperature dependence of the standard entropy of gas phase oxygen[49]. We have again assumed that oxygen loses all entropy upon adsorption. Furthermore, we assume that the reaction enthalpy is independent of temperature and coverage.) Figure 4.6b shows the resulting stability diagram. The extrapolation of our vacuum results to catalytically relevant pressures shows that the needle phase should be stable up to around 560 K for 1 mbar O_2 and even to 690 K in 1 bar. Hence, from the thermodynamic point of view Au surface oxides can be expected over the whole range of relevant temperatures for Au-based oxidation catalysis. However, reaction kinetics may play a vital role in determining the actual

oxide coverage under catalytic conditions. Hence, our predictions should serve as a starting point for further investigation.

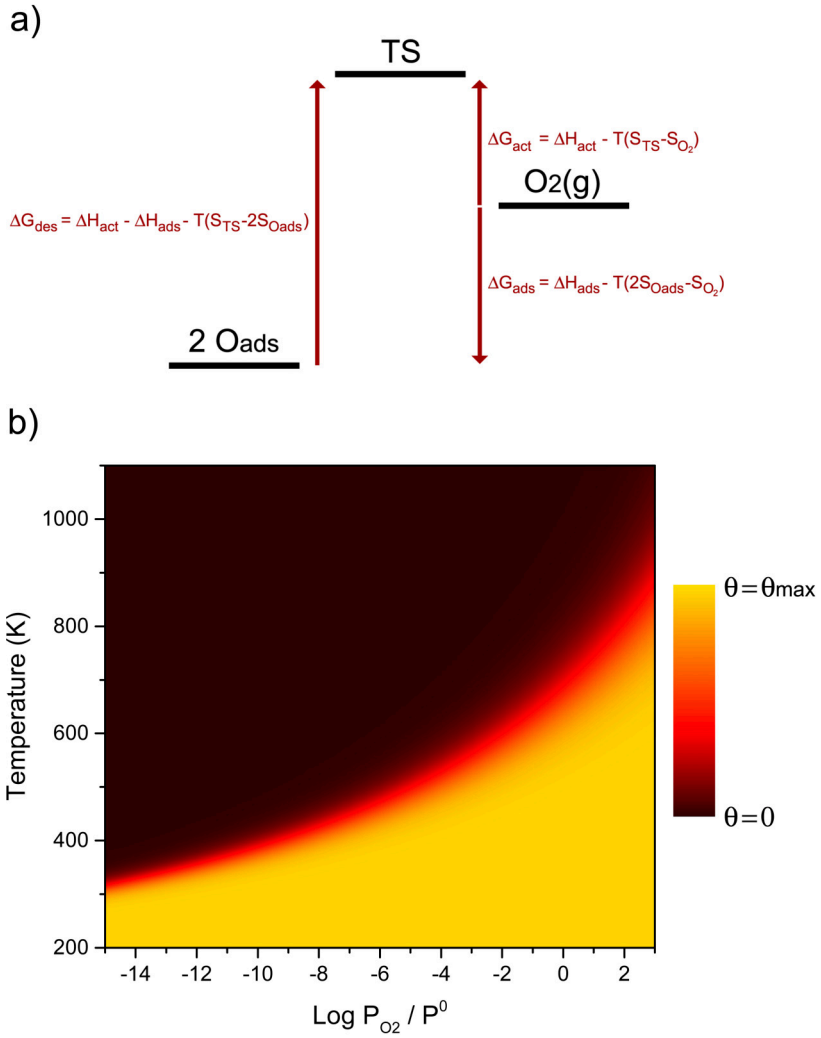

Figure 4.6: a) Components of the free energy of adsorption/desorption. "TS" designates the transition state. b) Stability diagram for the needle type Au surface oxide, based on equations 4.3, 4.4 and the experimentally derived adsorption enthalpy of -1.6 eV/O_2 molecule.

We should stress that the yellow regime in the diagram of Figure 4.6b presents a conservative estimate for the range of thermodynamic stability of surface oxides on Au(111). For the calculation of the reaction enthalpy, we have assumed that the system was in equilibrium. Since the oxygen in the gas phase is at room temperature, whereas the oxygen on the surface is at 423 K, we are actually underestimating the

stability of the oxide somewhat. Furthermore, some oxygen may have been lost during the cooling down of the crystal in vacuum. Moreover, if the assumption of negligible entropy of the adsorbed oxygen was incorrect, one may expect the stability at temperatures above 423 K to be improved, (while at lower temperatures the stability is reduced). Finally, we should point out that there may be Au surface oxide phases that are more stable than those reported here, but that would require the combination of high temperature and high pressure to overcome the kinetic limitations of their formation. Indeed, surface oxides with full coverage have been reported following preparation at 1073 K in 1 bar O_2[51]. As can be seen in Figure 4.6b, the needle phase is not stable under those conditions. This signifies the need to perform high-pressure, high-temperature experiments to further expand our understanding of the stability of Au surface oxides.

The activation barrier for oxygen adsorption via gold oxide can be estimated from a comparison between the oxide formation enthalpy and the desorption free energy barrier (see Figure 4.6a). A value of 1.43 eV was obtained for the latter from temperature programmed desorption (TPD) of oxygen, using the same assumptions we employed above[32]. The desorption temperature in the TPD experiments is not affected by pre-annealing up to 420 K[52], showing that the surface structure is close to equilibrium during the TPD runs. Hence, the desorption barrier found in TPD and the adsorption energy found in the present work relate to the same (equilibrated) state. We can insert the values for the desorption barrier (ΔG_{des}), the adsorption energy (ΔH_{ads}), and the desorption temperature (TPD peak at 550 K) in the following equation (see also Figure 4.6a):

$$\Delta G_{des} = \Delta H_{act} - \Delta H_{ads} - T(S_{TS} - 2S_{Oads}) \quad (4.5)$$

From this, it follows that the enthalpy barrier for adsorption (ΔH_{act}), is calculated as:

$$\Delta H_{act} = 550(S_{TS} - 2S_{Oads}) - 0.17 \quad (4.6)$$

Again, we assume that S_{Oads} = 0. Thus, ΔH_{act} only depends on the transition state entropy (S_{TS}). The first order kinetics observed in the TPD experiments[32,52] seem to indicate that the transition state does not correspond to the associative desorption of two oxygen atoms, but rather to the transition of an oxygen atom from the surface oxide to another adsorption state. For such a bound state, one may expect a small entropy (S_{TS}). Since S_{TS} is small, we conclude from Equation 4.6 that the enthalpy barrier for adsorption is also small or negligible. Hence, the free energy barrier for adsorption is mainly entropic. As a result, O_2 adsorption will be very efficient at mild temperatures and elevated pressures.

Although it is clear that Au surface oxides exhibit a strongly autocatalytic growth, one may wonder if a seed can be created on Au-reducible oxide catalysts under industrial conditions. Oxide-supported Au catalysts efficiently dissociate O_2 on the oxide support

or the Au-support perimeter, providing a source of atomic oxygen. It is unclear, however, whether the atomic oxygen can be transferred to the Au particle. For Ca contaminations in Au(111) this does appear to be possible, facilitating the formation of AuO_x using UHV O_2 exposure[53]. Similarly, traces of Ag are thought to aid in the oxidation of Au in nanoporous gold catalysts[54,55]. On the other hand, the present work shows that WO_3 and ReO_3 do not have the required properties to oxidize Au(111), even though they are well-known oxidation catalysts. Biener *et al.* also did not observe AuO_x on a TiO_x/Au(111) catalyst after O_2 exposure[56]. Thus, it seems that specific atomic arrangements are necessary to enable Au surface oxide formation.

Finally, we discuss how the presence of Au surface oxides could affect the overall reaction mechanism for Au-based oxidation catalysis. First, Au oxide provides an alternative pathway for O_2 dissociation besides dissociation on the support or at the Au-support perimeter. Whether or not this new pathway will be dominant, will depend on the amount of Au oxide present and the activity of the other pathways, which varies per type of catalyst. In the case where O_2 dissociation on Au oxide is not the dominant pathway, or when Au oxide is more stable at the Au-support perimeter[13], Au oxide will be predominantly located at the Au-support perimeter. Under such conditions, the reactivity will scale with the number of perimeter sites as was observed in several experiments[17,26]. Au oxide may also provide new sites for the adsorption of CO, which is rather weak on clean gold[19]. Finally, the Au oxide provides a low-energy[39] Mars van Krevelen type pathway for the reaction of CO with oxygen atoms.

4.4 Conclusion

Our results provide new evidence that Au surface oxides at the gas-surface interface of Au oxidation catalysts should be considered as a feasible reaction intermediate in a wide range of relevant temperatures and pressures. The experimentally derived formation enthalpy of -1.6 eV/O_2 molecule implies that surface oxides on Au(111) are thermodynamically stable up to approximately 560 K in 1 mbar O_2 and even up to 690 K in 1 bar. The presence of WO_3 and ReO_3 particles on the Au(111) substrate has little effect on the Au surface oxide structure, although a small attractive interaction was found.

While the Au surface oxides are stable even in low oxygen pressures, we find that WO_3 and ReO_3 are not able to facilitate their initial formation. When AuO_x seeds are provided however, Au surface oxide formation is facile. By comparison to literature temperature programmed desorption results we find that the barrier for O_2 dissociation on Au oxides is modest and predominantly determined by entropic contributions, implying that adsorption will be efficient at mild temperatures and elevated pressures.

Several types of surface oxide can be formed, depending on the employed conditions. In vacuum at room temperature our O_2/O mixture yields a disordered, rough surface. A similar exposure at 423 K yields a one-dimensional needle-type oxide. Experiments at a catalytically relevant pressure of 500 mbar O_2 revealed a highly dynamic surface where islands of a densely packed oxide develop. For the structure of this densely packed phase, we propose a model containing parallel Au oxide chains, analogous to those observed on Pt(111). The variety of observed Au oxide structures highlights their flexible bonding nature, which implies that Au surface oxides are likely not only stable on the (111) surface orientation, but also on other orientations present on Au nanoparticles.

References

[1] B.K. Min, C.M. Friend, Heterogeneous gold-based catalysis for green chemistry: Low-temperature CO oxidation and propene oxidation, Chem. Rev. 107 (2007) 2709–2724.

[2] M.D. Hughes, Y.J. Xu, P. Jenkins, P. McMorn, P. Landon, D.I. Enache, A.F. Carley, G.A. Attard, G.J. Hutchings, F. King, others, Tunable gold catalysts for selective hydrocarbon oxidation under mild conditions, Nature. 437 (2005) 1132–1135.

[3] C. Della Pina, E. Falletta, M. Rossi, Update on selective oxidation using gold, Chem. Soc. Rev. 41 (2012) 350–369.

[4] R. Ciriminna, E. Falletta, C. Della Pina, H. Teles, M. Pagliaro, Industrial Applications of Gold Catalysis, Angew. Chemie - Int. Ed. 55 (2016) 14210–17.

[5] N. Lopez, J.K. Nørskov, Catalytic CO oxidation by a gold nanoparticle: A density functional study, J. Am. Chem. Soc. 124 (2002) 11262–11263.

[6] G. Mills, M.S. Gordon, H. Metiu, Oxygen adsorption on Au clusters and a rough Au(111) surface: The role of surface flatness, electron confinement, excess electrons, and band gap, J. Chem. Phys. 118 (2003) 4198–4205.

[7] B. Yoon, H. Häkkinen, U. Landman, Interaction of O2 with Gold Clusters: Molecular and Dissociative Adsorption, J. Phys. Chem. A. 107 (2003) 4066–4071.

[8] M. Valden, S. Pak, X. Lai, D.W. Goodman, Structure sensitivity of CO oxidation over model Au/TiO2 catalysts, Catal. Letters. 56 (1998) 7–10.

[9] M. Haruta, Spiers Memorial Lecture : Role of perimeter interfaces in catalysis by gold nanoparticles, Faraday Discuss. 152 (2011) 11–32.

[10] A.Y. Klyushin, M.T. Greiner, X. Huang, T. Lunkenbein, X. Li, O. Timpe, M. Friedrich, M. Hävecker, A. Knop-Gericke, R. Schlögl, Is Nanostructuring Sufficient to Get Catalytically Active Au?, ACS Catal. 6 (2016) 3372–3380.

[11] J.C. Fierro-Gonzalez, B.C. Gates, Catalysis by gold dispersed on supports: the importance of cationic gold., Chem. Soc. Rev. 37 (2008) 2127–34.

[12] L.B. Vilhelmsen, Identi fi cation of the Catalytic Site at the Interface Perimeter of Au Clusters on Rutile TiO2(110), ACS Catal. 4 (2014) 1626–1631.

[13] L.B. Vilhelmsen, B. Hammer, Interfacial oxygen under TiO2 supported Au clusters revealed by a genetic algorithm search, J. Chem. Phys. 139 (2013) 204701.

[14] J.T. Miller, A.J. Kropf, Y. Zha, J.R. Regalbuto, L. Delannoy, C. Louis, E. Bus, J.A. van Bokhoven, The effect of gold particle size on Au{single bond}Au bond length and reactivity toward oxygen in supported catalysts, J. Catal. 240 (2006) 222–234.

[15] S. Minicò, S. Scirè, C. Crisafulli, A.M. Visco, S. Galvagno, FT-IR study of Au/Fe2O3 catalysts for CO oxidation at low temperature, Catal. Letters. 47 (1997) 273–276.

[16] M.S. Chen, D.W. Goodman, The structure of catalytically active Au on titania, Science 306 (2004) 252–255.

[17] T. Fujitani, I. Nakamura, Mechanism and active sites of the oxidation of CO over Au/TiO2, Angew. Chemie - Int. Ed. 50 (2011) 10144–10147.

[18] L.M. Liu, B. Mcallister, H.Q. Ye, P. Hu, Identifying an O2 Supply Pathway in CO

Oxidation on Au/TiO2(110): A Density Functional Theory Study on the Intrinsic Role of Water, J. Am. Chem. Soc. 128 (2006) 4017–4022.
[19] Z. Zeng, J. Greeley, Theoretical study of CO adsorption on Au catalysts under environmental catalytic conditions, Catal. Commun. 52 (2014) 78–83.
[20] H. Hartshorn, C.J. Pursell, B.D. Chandler, Adsorption of CO on Supported Gold Nanoparticle Catalysts: A Comparative Study, J. Phys. Chem. C. 113 (2009) 10718–10725.
[21] T. Yan, D.W. Redman, W.-Y. Yu, D.W. Flaherty, J. a. Rodriguez, C.B. Mullins, CO oxidation on inverse Fe2O3/Au(111) model catalysts, J. Catal. 294 (2012) 216–222.
[22] M.M. Schubert, S. Hackenberg, A.C. van Veen, M. Muhler, V. Plzak, R.J. Behm, CO Oxidation over Supported Gold Catalysts—"Inert" and "Active" Support Materials and Their Role for the Oxygen Supply during Reaction, J. Catal. 197 (2001) 113–122.
[23] Y. Chen, P. Crawford, P. Hu, Recent advances in understanding CO oxidation on gold nanoparticles using density functional theory, Catal. Letters. 119 (2007) 21–28.
[24] H. Koga, K. Tada, M. Okumura, Chemical Physics Letters DFT study of CO oxidation over Au/TiO2(110): The extent of the reactive perimeter zone, Chem. Phys. Lett. 610-611 (2014) 76–81.
[25] G.C. Bond, D.T. Thompson, Gold-Catalysed Oxidation of Carbon Monoxide, Gold Bull. 33 (2000) 41–50.
[26] M. Kotobuki, R. Leppelt, D.A. Hansgen, D. Widmann, R.J. Behm, Reactive oxygen on a Au/TiO2 supported catalyst, J. Catal. 264 (2009) 67–76.
[27] T.A. Baker, B. Xu, X. Liu, E. Kaxiras, C.M. Friend, Nature of Oxidation of the Au (111) Surface : Experimental and Theoretical Investigation, J. Phys. Chem. C Lett. 113 (2009) 16561–16564.
[28] T.A. Baker, C.M. Friend, E. Kaxiras, Effects of chlorine and oxygen coverage on the structure of the Au(111) surface, J. Chem. Phys. 130 (2009) 084701.
[29] H. Shi, C. Stampfl, First-principles investigations of the structure and stability of oxygen adsorption and surface oxide formation at Au(111), Phys. Rev. B. 76 (2007) 075327.
[30] K. Sun, M. Kohyama, S. Tanaka, S. Takeda, Structures and stabilities of gold oxide films on gold surfaces in O2 atmosphere, Surf. Sci. 628 (2014) 41–49.
[31] Z. Duan, G. Henkelman, CO oxidation at the Au/TiO2 boundary: The role of the Au/Ti5c site, ACS Catal. 5 (2015) 1589–95.
[32] X. Deng, B.K. Min, A. Guloy, C.M. Friend, Enhancement of O2 Dissociation on Au (111) by Adsorbed Oxygen : Implications for Oxidation Catalysis, J. Am. Chem. Soc. 127 (2005) 9267–9270.
[33] V. Schwartz, D.R. Mullins, W. Yan, B. Chen, S. Dai, S.H. Overbury, XAS Study of Au Supported on TiO2 : Influence of Oxidation State and Particle Size on the Catalytic Activity, J. Phys. Chem. B. 108 (2004) 15782–15790.
[34] P. Jiang, S. Porsgaard, F. Borondics, M. Kober, A. Caballero, H. Bluhm, F. Besenbacher, M. Salmero, Room-temperature reaction of oxygen with gold: An in situ ambient-pressure x-ray photoelectron spectroscopy investigation, J.

Am. Chem. Soc. 132 (2010) 2858–2859.
[35] C.T. Herbschleb, P.C. van der Tuijn, S.B. Roobol, V. Navarro, J.W. Bakker, Q. Liu, D. Stoltz, M.E. Cañas-Ventura, G. Verdoes, M.A. van Spronsen, M. Bergman, L. Crama, I. Taminiau, A. Ofitserov, G.J.C. van Baarle, J.W.M. Frenken, The ReactorSTM: atomically resolved scanning tunneling microscopy under high-pressure, high-temperature catalytic reaction conditions., Rev. Sci. Instrum. 85 (2014) 083703.
[36] R. V. Mom, M.J. Rost, J.W.M. Frenken, I.M.N. Groot, Tuning the Properties of Molybdenum Oxide on Al2O3/NiAl(110): Metal versus Oxide Deposition, J. Phys. Chem. C. 120 (2016) 19737–19743.
[37] Z.P. Liu, P. Hu, A. Alavi, Catalytic role of gold in gold-based catalysts: A density functional theory study on the CO oxidation on gold, J. Am. Chem. Soc. 124 (2002) 14770–14779.
[38] B.K. Min, A.R. Alemozafar, M.M. Biener, J. Biener, C.M. Friend, Reaction of Au(111) with Sulfur and Oxygen: Scanning Tunneling Microscopic Study, Top. Catal. 36 (2005) 77–90.
[39] B.K. Min, A.R. Alemozafar, D. Pinnaduwage, X. Deng, C.M. Friend, Efficient CO Oxidation at Low Temperature on Au(111), J. Phys. Chem. B. 110 (2006) 19833–19838.
[40] N. Fairley, CasaXPS 2.3, (1999). www.casaxps.com.
[41] P.J. Cumpson, M.P. Seah, Elastic Scattering Corrections in AES and XPS. II. Estimating Attenuation Lengths and Conditions Required for their Valid Use in Overlayer/Substrate Experiments, Surf. Interface Anal. 25 (1997) 430–446.
[42] J.V. V. Barth, H. Brune, G. Ertl, R.J. Behm, Scanning tunneling microscopy observations on the reconstructed Au(111) surface: atomic structure, lon-range superstructure, rotational domains, and surface defects, Phys. Rev. B. 42 (1990) 9307–9318.
[43] P.G. Lusteinberg, C. Vericat, G.A. Benitez, M.E. Vela, N. Tognalli, A. Fainstein, M.L. Martiarena, R.C. Salvarezza, Spontaneously formed sulfur adlayers on gold in electrolyte solutions: Adsorbed sulfur or gold sulfide?, J. Phys. Chem. C. 112 (2008) 11394–11402.
[44] J.M. Hawkins, J.F. Weaver, A. Asthagiri, Density functional theory study of the initial oxidation of the Pt(111) surface, Phys. Rev. B. 79 (2009) 125434.
[45] D.J. Miller, H. Øberg, S. Kaya, H. Sanchez Casalongue, D. Friebel, T. Anniyev, H. Ogasawara, H. Bluhm, L.G.M. Pettersson, A. Nilsson, Oxidation of Pt(111) under near-ambient conditions, Phys. Rev. Lett. 107 (2011) 195502.
[46] S.P. Devarajan, J.A. Hinojosa, J.F. Weaver, STM study of high-coverage structures of atomic oxygen on Pt(111): p(2x1) and Pt oxide chain structures, Surf. Sci. 602 (2008) 3116–3124.
[47] M.A. van Spronsen, Oxidation catalysis on Pt and Au, Leiden University, 2016.
[48] T.M. Pedersen, W. Xue Li, B. Hammer, Structure and activity of oxidized Pt(110) and alpha-PtO2., Phys. Chem. Chem. Phys. 8 (2006) 1566–74.
[49] NIST, Computational Chemistry Comparison and Benchmark Database, (2016). http://cccbdb.nist.gov/.
[50] H. Ibach, Physics of Surfaces and Interfaces, Springer, Berlin, 2006.

[51] L. Huang, P. Zeppenfeld, J. Chevrier, G. Comsa, Surface morphology of Au(111) after exposure to oxygen at high temperature and pressure, Surf. Sci. 352-354 (1996) 285–289.
[52] R.A. Ojifinni, J. Gong, D.W. Flaherty, T.S. Kim, C.B. Mullins, Annealing effect on reactivity of Oxygen-Covered Au(111), J. Phys. Chem. C. 113 (2009) 9820–9825.
[53] M. E. Schrader, Chemisorption of oxygen to gold: AES study of catalytic effect of calcium, Surf. Sci. 78 (1978) L227–L232.
[54] J. Biener, M.M. Biener, R.J. Madix, C.M. Friend, Nanoporous Gold: Understanding the Origin of the Reactivity of a 21st Century Catalyst Made by Pre-Columbian Technology, ACS Catal. 5 (2015) 6263–6270.
[55] L. V. Moskaleva, T. Weiss, T. Klüner, M. Bäumer, Chemisorbed Oxygen on the Au(321) Surface Alloyed with Silver: A First-Principles Investigation, J. Phys. Chem. C. 119 (2015) 9215–9226.
[56] J. Biener, E. Farfan-Arribas, M. Biener, C.M. Friend, R.J. Madix, Synthesis of TiO2 nanoparticles on the Au(111) surface., J. Chem. Phys. 123 (2005) 094705.

Chapter 4 – Supporting information

The growth and stability of Au surface oxides on WO_3/Au(111) and ReO_3/Au(111) inverse model catalysts

4.5 Reduction and surface alloying of WO_3 at elevated temperature

To study the stability of WO_3 on the Au(111) surface, we conducted a series of experiments at elevated temperatures. Figure 4.7a and b show 0.03 ML WO_3/Au(111) before and after annealing to 567 K in vacuum. Before annealing, we associate the bright features with WO_3 and the dark lines with the needle type Au surface oxide, similar to Figure 4.4 in the main text. After annealing, only 0.008 ML WO_x is visible in

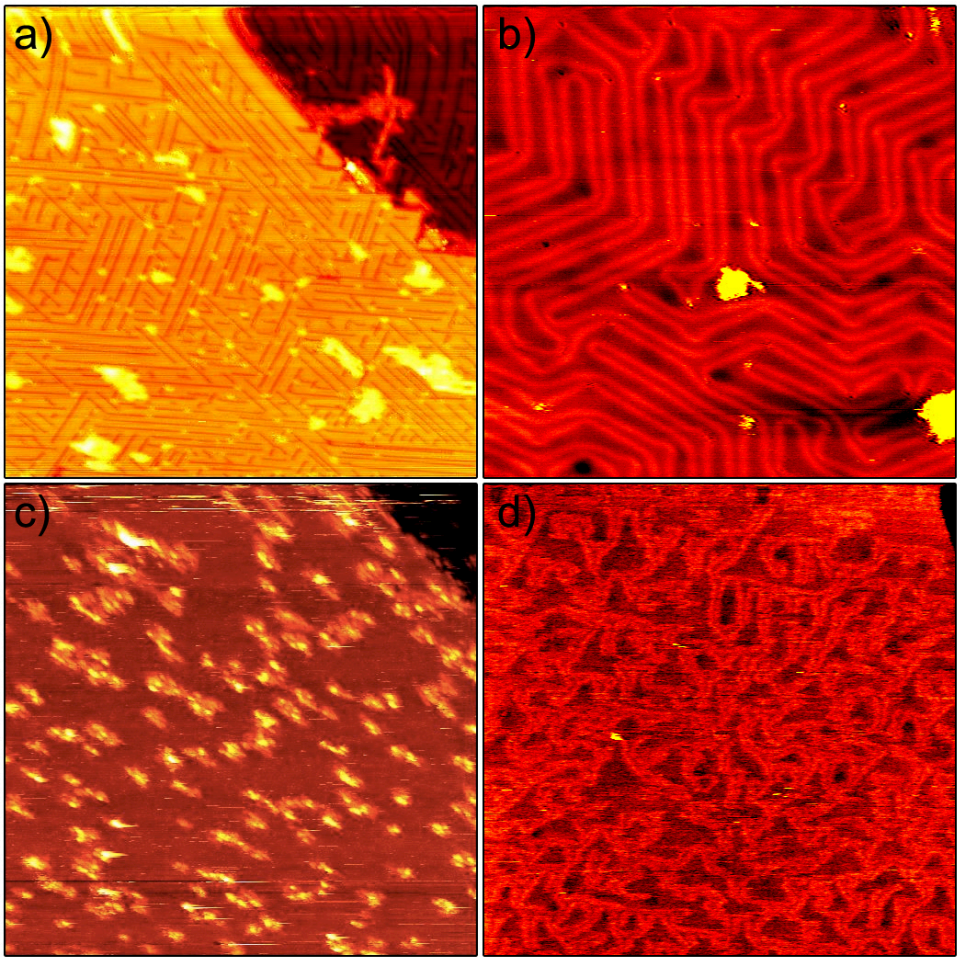

Figure 4.7: Surface alloying of WO_3/Au(111) at elevated temperature. a) 0.03 ML WO_3/Au(111) prepared by WO_3 deposition at 567 K in $1x10^{-5}$ mbar O_2 and cooling to 400 K in O_2, 80 nm x 80 nm, U_s = 2 V, I_t = -135 pA. b) Sample in a) after annealing at 567 K in vacuum, 80 nm x 80 nm, U_s = 2 V, I_t = -110 pA. c) 0.2 ML WO_3/Au(111) prepared by W deposition at room temperature, followed by annealing in 1 bar O_2 for 1 hour, 80 nm x 80 nm, U_s = 2 V, I_t = -90 pA. d) same as c), after annealing at 653 K in $5x10^{-6}$ mbar O_2, 160 nm x 160 nm, U_s = -1V, I_t = 30 pA

the STM images (see Figure 4.7 b), even though sublimation is not expected at the mild annealing temperature employed here. Alternatively, surface alloying of W with the gold may have occurred. The dark stains in the fcc areas of the herringbone reconstruction in Figure 4.7b suggest that a W-Au alloy is indeed formed. The surface alloying process is even more pronounced in experiments with a higher WO_3 coverage, as shown in Figures 4.7c and d. The sample for this experiment was prepared via the deposition of approximately 0.2 ML W metal and subsequent oxidation in 1 bar O_2 at 523 K for 1 hour. This results in the structure shown in Figure 4.7c. After annealing to 653 K in $5x10^{-6}$ mbar O_2, no particles are visible on the surface and the herringbone reconstruction is strongly modified (see Figure 4.71d). Again, this points at the formation of a surface alloy. The larger amount of tungsten present on the surface allows for a stronger modification of the herringbone reconstruction. The observation that the surface alloying even occurs in the presence of oxygen shows that the tungsten oxide is not only kinetically instable at high temperature in vacuum, but also thermodynamically unstable at modest oxygen chemical potential (μ_O=-2.46 eV under the applied conditions).

4.6 X-ray beam induced desorption of surface oxides

Damage to adsorption structures due to (photo)electrons is a well-known phenomenon in surface science. However, due to its comparatively low electron flux, lab source X-ray photoelectron spectroscopy (XPS) is usually less prone to beam damage effects. In our case, the X-ray beam spot on the sample had a diameter of approximately 4 mm, inducing a sample current of 1.1 nA. Thus, in the 2.5 hours of X-ray exposure that we needed for the experiment, only 0.35 photoelectron per Au surface atom left the surface.

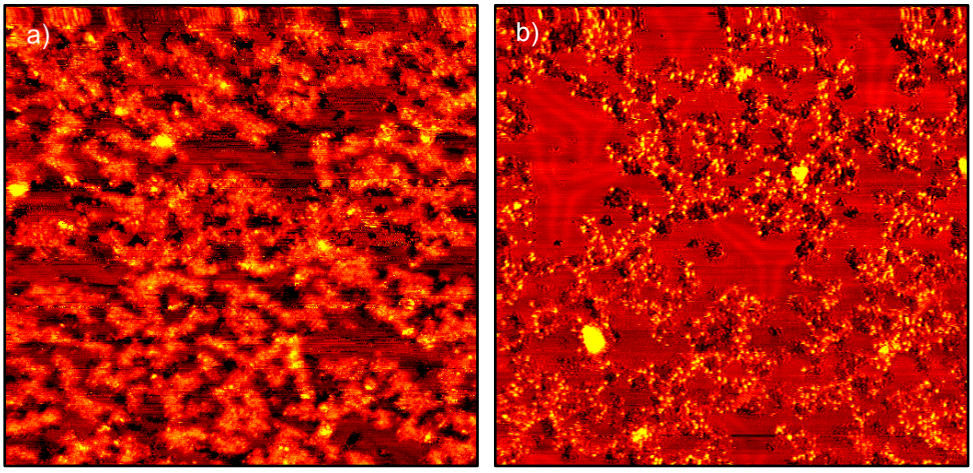

Figure 4.8: 0.012 ML ReO_3/Au(111) before (a) and after (b) XPS measurements. a) 80 nm x 80 nm, U_s = -1V, I_t = 50 pA. b) 80 nm x 80 nm, U_s = -1 V, I_t = 50 pA

Figure 4.8 shows that even under this very mild radiation load, substantial beam-induced oxygen desorption occurs. This indicates that synchrotron measurements, which employ a beam flux that is several orders of magnitude larger, need to be performed with the greatest of care. In our case, the O 1s spectrum was recorded within the first 45 minutes of the measurement. Nonetheless, one may expect that the measured signal intensity was affected by the beam-induced desorption.

4.7 Evolution of WO_3/Au(111) during pressure ramp to 500 mbar O_2

The starting structure for the high-pressure experiment shown in this section was formed by exposure of a WO_3/Au(111) sample to $1x10^{-5}$ mbar O_2/O at room temperature, followed by annealing at 500 K to partially smoothen the surface. The oxygen atmosphere was maintained until the sample temperature was back below 423K. The resulting surface structure contains modest amounts of AuO_x, which we associate with the bright features in Figure 4.9a. Furthermore, vacancy islands are apparent.

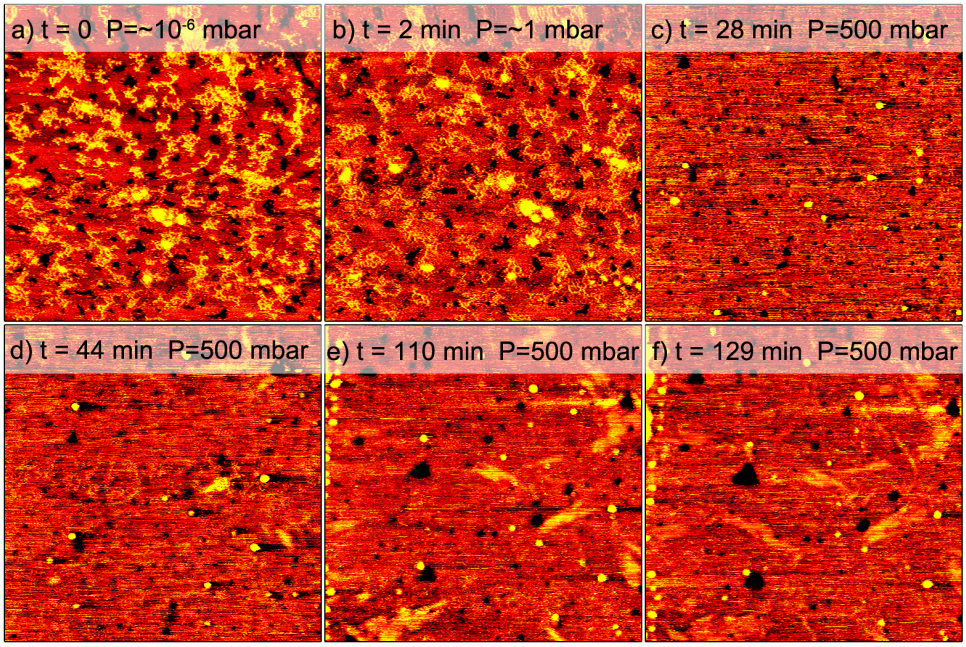

Figure 4.9: Structural evolution of WO_3/Au(111) during high-pressure oxygen exposure at room temperature. Panels a) and b): 80 nm x 80 nm, other panels: 160 nm x 160 nm. All frames are recorded at U_s = 2 V and I_t = -170 pA. All indicated pressures refer to oxygen.

Following the preparation, the surface was imaged at room temperature while the O_2 pressure was increased from 10^{-6} mbar to 500 mbar. The lower bound, 10^{-6} mbar, is an estimate that corresponds to the situation where the reactor is only connected to the UHV chamber via thin gas lines. Under these conditions, there is a poorly defined vacuum inside the reactor. When the gas lines are switched from the mode in which they connect to the UHV system to the mode in which they connect to the high-pressure gas supply, the pressure jumps to approximately 1 mbar. Figure 4.9b shows that the bright species from Figure 4.9a become less apparent after this pressure increase. The surface morphology is maintained. While we further increased the pressure, the images became streaky (see Figure 4.9c), indicating that there are dynamic species present on the surface. The bright species disappear nearly completely, which we interpret as their dissolution in the dynamic phase on the terraces. Subsequently, islands with highly anisotropic shapes emerge, which we associate with AuO_x. The nucleation of these islands seems to occur at random locations on the surface, without preference for steps or vacancy islands. Note that the number of islands formed and the rate of their formation may have been affected by the STM tip. The row of particles on the left-hand side in Figures 4.9e and 4.9f indicate that atoms have been moved to the side of the imaging area. In other high-pressure experiments, we noted that instabilities in the tunneling caused the formation of vacancy islands. This again signifies the dynamic nature of the Au surface when adsorbed oxygen is present. Images recorded immediately after moving to previously unimaged areas ensured that the formation of the surface oxide islands occurs everywhere on the surface. The images obtained in UHV after the high-pressure exposure, described in the main text, corroborate this.

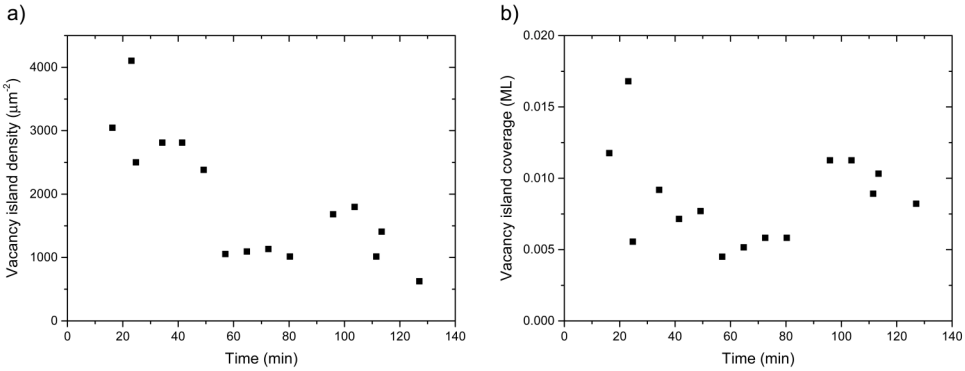

Figure 4.10: Evolution of vacancy islands during the high-pressure experiment shown in Figure 4.9.

During the high-pressure experiment, it is clear that some vacancy islands grow in size. Meanwhile, the number of vacancy islands clearly decreases, as shown in Figure 4.10a. Since the "center of mass" of the vacancy islands remains constant, we conclude that Ostwald ripening occurs. In vacuum, the vacancy islands were stable. Hence, the adsorbed oxygen at high-pressures must induce an increased mobility of vacancies

over the terraces. Figure 4.10b shows that the total vacancy island area remains constant during the experiment, although the measured values scatter around the average with a standard deviation of 37%. This large scatter results from the streakiness of the images, which hampers proper quantification. As noted in the main text, a constant vancancy island density implies that gold adatoms are not part of the dynamic phase on the terraces, because these would have filled the vacancies. In the experiment shown in Figure 4.9, we did not observe the formation of new vacancy islands, which indicates that no Au adatoms are required for the formation of the AuO_x islands.

4.8 Influence of the preparation conditions on the structure and coverage of the needle phase Au oxide

The needle type oxide was generated via two methods. In the first, WO_3 or ReO_3 was deposited at 567 K in $1x10^{-5}$ mbar O_2, after which the sample was allowed to cool down over the course of several minutes to 423 K in $1x10^{-5}$ mbar O_2/O. Figure 4.4 in the main text shows the result of this procedure. We note however that the coverage obtained is sensitive to the exact preparation conditions, as is evidenced by Figure 4.11a. The surface was prepared using the same procedure as in Figure 4.4 in the main text, yet the observed Au oxide needle coverage is clearly lower. One may wonder therefore whether the surface truly equilibrates during the cooling down to 400 K. To resolve this, we prepared the needle phase via a second procedure. WO_3 was

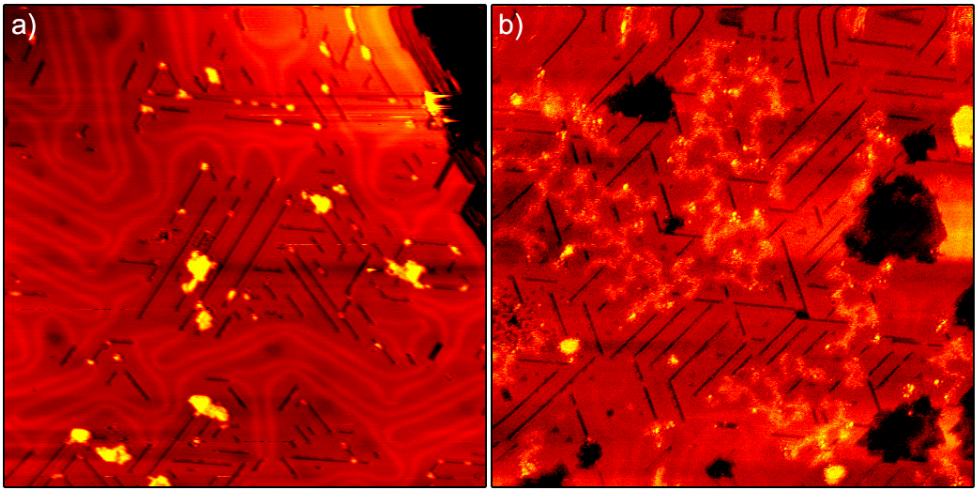

Figure 4.11: Influence of the preparation conditions on the Au needle oxide coverage. a) WO_3/Au(111) prepared through WO_3 deposition at 567 K, followed by cooling to 423 K in $1x10^{-5}$ mbar O_2/O. 80 nm x 80 nm, U_s = 2 V, I_t = -95 pA. b) WO_3/Au(111) prepared through WO_3 deposition at room temperature, followed by 15 minutes $1x10^{-5}$ mbar O_2/O exposure, 15 minutes annealing to 423 K in vacuum, and 15 minutes $1x10^{-5}$ mbar O_2/O exposure at 423 K. 80 nm x 80 nm, U_s = 1.5 V, I_t = -160 pA.

deposited at room temperature in $1x10^{-5}$ mbar O_2, followed by 15 minutes of $1x10^{-5}$ mbar O_2/O exposure. After this, the surface was annealed at 423 K in vacuum for 15 minutes to smoothen the surface, followed by 15 minutes of $1x10^{-5}$ mbar O_2/O exposure at 423 K to generate an equilibrium coverage of Au oxide needles. As can be seen in Figure 4.11b, this results in an oxide needle coverage similar to that in Figure 4.4. Thus, we conclude that the surface in Figure 4.4 was equilibrated with the conditions at 423 K. A possible explanation why we do not always reach equilibrium, such as in Figure 4.11a, could be a variation in the distance between the filament and the sample. The flux of atomic oxygen to the surface depends quadratically on the filament-sample distance. Hence, variations in this distance may generate strong variations in the amount of AuO_x nuclei that are generated. As a result, the time required to reach equilibrium will fluctuate. Another source of variation is the cooling rate, which was not actively controlled in the experiments.